J Nanopart Res (2017) 19:114
DOI 10.1007/s11051-017-3820-z

BRIEF COMMUNICATION

Optimized permeation and antifouling of PVDF hybrid ultrafiltration membranes: synergistic effect of dispersion and migration for fluorinated graphene oxide

Mingming Li · Jie Shi · Cheng Chen · Nan Li · Zhiwei Xu · Jing Li · Hanming Lv · Xiaoming Qian · Xiaoning Jiao

Received: 21 July 2016 / Accepted: 5 March 2017

Abstract Nanoparticles may have suffered from low modification efficiency in hybrid membranes due to embedding and aggregating in polymer matrix. In order to analyze the modification mechanisms of nanoparticle migration and dispersion on the properties of hybrid membranes, we designed different *F*/*O* ratios ($R_{F/O}$) of fluorinated graphene oxide (FGO, diameter = 1.5 ~ 17.5 μm) by carbon tetrafluoride (CF_4) plasma treatment GO for 3, 5, 10, 15, and 20 min and successfully prepared novel PVDF hybrid membranes containing FGO via the phase inversion method. After a prolonged plasma treatment, the $R_{F/O}$ of FGO was enhanced sharply, indicating an increasing compatibility of FGO with the matrix, especially FGO-20 (GO treated for 20 min). FGO contents in the top layer, sublayer, and the whole of membranes were probed by X-ray photoelectron spectroscopy, energy-dispersive spectrometer, and indirect computation, respectively. In the top layer of membranes, FGO contents declined from 13.14 wt% (PVDF/GO) to 4.00 wt% (PVDF/FGO-10) and 1.96 wt% (PVDF/FGO-20) due to the reduced migration ability of FGO. It is worth mentioning that PVDF/FGO-10 membranes exhibited an excellent water flux and flux recovery rate (up to 406.90 L m^{-2} h^{-1} and 88.9%), which were improved by 67.3% and 14.6% and 52.5% and 24.0% compared with those of PVDF/GO and PVDF/FGO-20 membranes, respectively, although the dispersion and migration ability of FGO-10 was maintained at a moderate level. It indicated that the migration and dispersion of FGO in membranes could result in dynamic equilibrium, which played a key role in making the best use of nanomaterials to optimize membrane performance.

Keywords Fluorinated graphene oxide · Ultrafiltration membranes · Dispersion · Migration · Optimal performance · Polymeric membranes with nanoparticles

Introduction

Polymeric ultrafiltration membranes are widely used in membrane separation processes due to their low cost, easily controlled morphology, and excellent mechanical properties (Yeow et al. 2004; Tan et al. 2006). Unfortunately, the hydrophobicity of polymer such as polyvinylidene fluoride (PVDF), polypropylene, and polysulfone always accumulates adsorptions or depositions between membrane surfaces and organic foulants (pathogens, proteins, etc.) in impaired water (Liu et al. 2015b), which subsequently decreases permeation flux. In recent years, researchers have done a lot of work to improve the performance of membranes and found that adding inorganic nanomaterial into membranes such as

Mingming Li and Jie Shi contributed equally to this work.

Electronic supplementary material The online version of this article (doi:10.1007/s11051-017-3820-z) contains supplementary material, which is available to authorized users.

M. Li · J. Shi · C. Chen · N. Li · Z. Xu (✉) · J. Li · H. Lv · X. Qian (✉) · X. Jiao
State Key Laboratory of Separation Membranes and Membrane Processes, School of Textiles, Tianjin Polytechnic University, Tianjin 300387, China
e-mail: xuzhiwei@tjpu.edu.cn
e-mail: qianxiaoming@tjpu.edu.cn

Published online: 17 March 2017

TiO_2 (Goh et al. 2014; Zhang et al. 2016), ZnO (Hong and He 2014; Liang et al. 2012), SiO_2 (Li et al. 2016; Zhu et al. 2016), ZrO_2(Pang et al. 2014), Al_2O_3 (Wang et al. 2016), carbon nanotubes, and graphene oxide (Meng et al. 2016; Wang et al. 2012c) could bring a new concept to fabricate excellent water treatment membranes with high water flux, high solute rejection, or low fouling properties. The reason was that the blend polymers and nanomaterials with size less than 100 nm might give rise to the quantum size effect by yielding new polymer/particle interfacial areas, hence modifying the intrinsic properties of nanomaterials (Goh et al. 2014; Jiang et al. 2014; Vatanpour et al. 2012; Wang et al. 2012a). But there were still many confusing problems, such as the effect mechanisms of nanomaterials on the property of hybrid membranes, which could affect the optimal design of membrane properties.

Zhu et al. (2015) used SiO_2 nanoparticles with good dispersibility to enhance the fouling resistance of hydrophobic materials within a zwitterionic medium. Wu et al. (2010) concluded that using triethanolamine as the crosslinking agent would increase dispersion of multi-walled carbon nanotubes in the membrane. Amine-functionalized multi-walled carbon nanotubes could be used to improve their dispersion capabilities and antifouling property of membranes (Ahmad Rahimpour et al. 2012). In our previous work (Ma et al. 2013; Xu et al. 2014; Zhang et al. 2013b, 2013c; Zhao et al. 2013c), we had also simply investigated the influence of different blending proportions of oxidized carbon nanotubes and graphene oxide (GO) on permeation and antifouling performance of ultrafiltration membranes, and the results indicated that the stack of GO was effectively inhibited by introducing oxidized carbon nanotubes. Improving the dispersion of nanomaterials was conducive to membrane properties, but majority of nanomaterials embedded in the membrane matrix and the properties of nanomaterials could not be truly exploited. In order to improve the nanomaterial content in the surface of membranes, migration behavior was an interesting and low-energy consumption process, which were reported by Jiang group (Chen et al. 2011; Liu et al. 2015b; Zhao et al. 2014) and other research groups (Asatekin et al. 2007; Hashim et al. 2009; Zhao et al. 2013b; Zhu et al. 2014b). María Arsuaga et al. (2013) explored the effect of the metal oxide nanoparticle aggregation. They reached two important conclusions: (a) an abrupt increase in size of the particles as a result of dispersion into the polymeric solution would tend to impede a uniform distribution of the particles and (b) strong correlation was found between membrane fouling resistance and the spatial distribution of particles inside the membrane structure. The higher number of particles was in membrane surface, the more hydrophilic membrane was formed. The above researches indicated that the properties of hybrid membranes were influenced by both the dispersion and migration of nanomaterials. However, a few people carried on the concrete research about the effect of nanomaterial dispersion and migration on organic–inorganic hybrid membrane performance.

Based on previous studies, we treated GO using CF_4 plasma to synthesize FGO with different *F*/*O* ratios, which had different dispersion and migration abilities. Then, PVDF/FGO hybrid ultrafiltration membranes were developed from the blending solution of PVDF and FGO nanoparticles via phase inversion method. For the dispersion of FGO, we tested the viscosity of PVDF/FGO casting solution. For the migration behavior of FGO and GO, we used X-ray photoelectron spectroscopy (XPS), energy-dispersive spectrometer (EDS), and indirect computation to probe or calculate oxygen and FGO contents in different depths of membranes. Permeability and antifouling properties of membranes were confirmed in terms of pure water flux, rejection, flux recovery rate, the membrane-foulant adhesion force, and others. Based on the above results, the optimization nanoparticle-modified hybrid ultrafiltration membranes were investigated.

Experimental

Materials

The PVDF (FR904) was purchased from Shanghai 3F New Materials Co., Ltd. China. Graphite was purchased from the Qingdao Ruisheng Graphite Co., Ltd. China. H_3PO_4, $KMnO_4$ (analytical grade), H_2SO_4 (98%), H_2O_2 aqueous solution (30%), *N*,*N*-dimethylacetamide (DMAc, >99.5%, reagent), polyvinyl pyrrolidone (PVP), and other common chemicals were purchased from Tianjin Weichen Chemical Reagent Co., Ltd. China. Distilled water was used as the nonsolvent for polymer precipitation.

Preparation of GO and FGO

GO powders were prepared by an improved Hummers' method (Shi et al. 2012). To form FGO, the microwave plasma etcher (YZ-Z) was employed to finish the process of fluorination at room temperature with the CF_4 flow. The degree of fluorination process was adjusted by controlling the exposure time (3, 5, 10, 15, 20 min) when the plasma was ignited, and these graphene nanosheets were named as FGO-3, FGO-5, FG0-10, FGO-15, and FGO-20, correspondingly. A detailed synthesis has been reported in our previous work (Zhou et al. 2015).

Preparation of membranes

The novel PVDF/FGO hybrid ultrafiltration membranes were prepared via immersion precipitation phase inversion-induced method. Casting solutions were prepared by dissolving PVDF, GO or FGO, and PVP in solvent DMAc. PVDF (15 wt% in casting solutions) was a membrane matrix, PVP (1 wt% in all casting solutions) was a pore-forming agent, GO or FGO (0.15 wt% in casting solutions) was a membrane-modified agent, and distilled water at room temperature was a nonsolvent coagulation bath. After dispersing FGO in DMAc, PVDF and PVP were dissolved in the dope solutions by continuous stirring at 323.15 K for 24 h. After fully degassing, the casting solution was spread onto clean glass plates with 220 μm gap and then immersed into coagulation bath (distilled water) for 30 min. After peeling off from glass plates, the resultant membranes were rinsed in distilled water before ultrafiltration tests. In order to identify these membranes easily, it was denoted as PVDF, PVDF/GO, and PVDF/FGO-n (n = 3, 5, 10, 15, and 20), respectively.

Compatibility and migration behavior of FGO in membranes

The viscosity of PVDF/FGO casting solution was measured with rotational rheometer (Bohlin CVO). The temperature of unit was controlled at 298.15 K by a circulating water system. The casting solution was placed in the cylinder, and sufficient time was allowed for it to reach thermal equilibrium. The shear stress was determined up to shear rates of 100 rpm. Each casting solution was tested five times to obtain the mean value. The top and bottom morphologies of membranes were characterized by scanning electron microscope (SEM) (Hitachi S-4800) after the samples were gold-sputtered. The surface chemical compositions of FGO and membranes such as C, O, and F were analyzed by XPS (Thermo ESCALAB 250) and EDS (JEOL JSM-5900LV), which have different detection depths (top layer and sublayer). And the FGO-n average contents in different depths of membranes were calculated indirectly according to formulas (7)–(9).

Permeability and antifouling properties of membranes

Pure water flux of membranes with an effective area of 19.3 cm^2 was conducted on a dead-end membrane system. Both the pure water flux and rejection tests were directed at 25 °C with a feed pressure of 0.1 MPa. The rejection was investigated with 1.0 g L^{-1} BSA solution using 0.1 M phosphate-buffered at pH 7.4. Concentrations of BSA in the permeation and feed solution were measured by UV spectrophotometer (Shimadzu UV-2450, Japan). Permeation flux and rejection were defined using the following equations, respectively:

$$J = \frac{Q}{A \times T} \tag{1}$$

$$R = \left(1 - \frac{C_P}{C_F}\right) \times 100\% \tag{2}$$

where Q (L) was the total volume penetrating through the membrane during the operation time T (h) with an effective filtration area of A (m^2). J was permeation flux of membranes for pure water (L m^{-2} h^{-1}). R was the rejection to BSA (%) using a UV spectrophotometer at 280 nm, and C_P and C_F were the concentrations of BSA in the permeation and feed solution, respectively.

For the fouling resistance analysis, the experiments included three filtration steps were conducted following the procedure according to our previous reports (Zhang et al. 2013b). Briefly, in the first step, the pure water permeability (Jw_0) was measured until the flux remained stable. Then, 1.0 g L^{-1} BSA solution was fed into the filtration system and the flux (Jp) was measured for 1 h. Then, the membranes were washed with distilled water for 30 min to remove pollutant on membrane pore wall or surface before measuring the water flux of the cleaned membranes (Jw_1).

To analyze the fouling process in detail, several equations were used to describe the fouling resistance of membranes. The total flux decline ratio (Rt), reversible flux decline ratio (Rr), irreversible flux decline ratio (Rir), and flux recovery rate (FRR) were defined and calculated as follows:

$$\mathrm{Rt}(\%) = \left(1 - \frac{\mathrm{Jp}}{\mathrm{Jw}_1}\right) \times 100 \quad (3)$$

$$\mathrm{Rr}(\%) = \left(\frac{\mathrm{Jw}_1 - \mathrm{Jp}}{\mathrm{Jw}_0}\right) \times 100 \quad (4)$$

$$\mathrm{Rir}(\%) = \left(\frac{\mathrm{Jw}_0 - \mathrm{Jw}_1}{\mathrm{Jw}_0}\right) \times 100 = \mathrm{Rt} - \mathrm{Rr} \quad (5)$$

$$\mathrm{FRR}(\%) = \frac{\mathrm{Jw}_1}{\mathrm{Jw}_0} \times 100 \quad (6)$$

The membrane surface morphology, in terms of the mean surface roughness (*Ra*) and root-mean-square roughness (*RMS*), was studied by AFM (CSPM5500). To further analyze the fouling process, the antifouling performance of different samples was observed by AFM under the tapping mode. The AFM tip was modified according to the procedure described elsewhere (Zhang et al. 2013c). We used BSA for the immobilization of a protein on the AFM tips. As membrane surface approached the BSA-immobilized AFM tip, an interaction was generated between the tip and membrane surface. The force could be detected in the same manner when the surface was retracted. A speed of 0.1 μm s^{-1} was applied to obtain the force–extension curves during approach and retraction of membrane surface from the BSA-immobilized tip. To minimize the experimental error and determine the force distribution, approximately 50 approach/retract cycles were conducted on the membrane surface for at least five locations, with 20 measurements at each location.

Results and discussion

Component of FGO and pristine GO

Figure 1a showed the XPS survey spectra of the GO and FGO-10. The detailed component analysis and nano scale features had been reported in our previous work (Zhou et al. 2015). On the XPS spectrum of FGO-10, a peak near 688 eV could be observed, suggesting an effective grafting of fluorine on the GO surface. Figure 1b showed the different *F*/*O* and *F*/*C* ratio ($R_{F/O}$ and $R_{F/C}$) of FGO by different plasma treatment time. It can be seen that $R_{F/O}$ and $R_{F/C}$ of FGO gradually increased with increasing treatment time, and the change of $R_{F/O}$ was especially obvious. These results confirmed that the $R_{F/C}$ and $R_{F/O}$ of FGO could be easily adjusted by controlling reaction conditions. Meanwhile, the size of GO did not change with plasma treatment, and the size range of GO (diameter = 1.5 ~ 17.5 μm) was observed with a laser particle size analyzer (Fig. S1).

Compatibility of FGO in casting solution

The compatibility of FGO with different $R_{F/O}$ in PVDF was measured by casting solution viscosity. The viscosity of neat PVDF casting solution was low because of no GO and FGO. For the nanoparticle-added casting solutions, stronger interconnection between the molecules revealed a higher viscosity (Zhang et al. 2013a; Greenlee and Rentz 2016). As shown in Tables 1 and S1, the mean values of the modified casting solution viscosity and the *F*/*O* and *F*/*C* ratios of hybrid membranes were gradually raised with the increase $R_{F/O}$ of FGO. F atoms were grafted onto the surface of GO, which significantly enhanced the degree of strong interaction and entanglement between FGO and PVDF polymer (Sukitpaneenit and Chung 2009). Therefore, the greater was $R_{F/O}$ of FGO, the better was FGO compatibility in casting solution. Apparently FGO-20 compatibility was the best in all system studied.

EDS was used to determine oxygen distribution of PVDF hybrid membranes. In order to improve the contrast, PVDF/GO, PVDF/FGO-10, and PVDF/FGO-20 membranes were chosen and analyzed. Figure 2a–c showed the oxygen distribution in PVDF/GO, PVDF/FGO-10, and PVDF/FGO-20 membrane surfaces. As shown in the area marked by the red line, the uniform distribution degree of surface oxygen existed in the following order: PVDF/FGO-20 > PVDF/FGO-10 >

Table 1 Viscosity of PVDF/FGO casting solution and the *F*/*O* and *F*/*C* ratios of membranes by XPS

Sample	Casting solution viscosity (mPa s)	Membrane	
		F/*O*	*F*/*C*
PVDF	1577 ± 5	11.12	0.67
PVDF/GO	1833 ± 11	3.51	0.44
PVDF/FGO-3	1848 ± 7	8.41	0.62
PVDF/FGO-5	1864 ± 6	8.69	0.65
PVDF/FGO-10	1898 ± 6	8.04	0.65
PVDF/FGO-15	1912 ± 5	9.07	0.66
PVDF/FGO-20	1914 ± 7	10.38	0.66

PVDF/GO (aggregation in yellow line). Similarly, the bottom morphology of PVDF/FGO membranes (Fig. S2) showed more uniform pore distribution than that of PVDF/GO membranes. All top surfaces seemed to be flat, but the smooth degree reduced with increasing $R_{F/O}$ of FGO, indicating that the structures of the top surface were altered by the addition of varying $R_{F/O}$ of FGO. Two factors were proposed to explain the change: (i) the enrichment of FGO on membrane surface (discussed below) and (ii) the strong interaction between FGO surface and PVDF chain which was in agreement with the results of Table 1 as discussed above.

Migration behavior of FGO

Figure 2d displayed the variation of oxygen content from inside to surface of PVDF/FGO-10, illustrating that the oxygen content of membrane surface was distributed more densely than that of membrane middle part. This indicated that the migration behavior of FGO-10 was obvious in the phase inversion process and meanwhile maintained good compatibility with PVDF, as shown in Fig. 2b. Previous results of literatures also demonstrated that the migration phenomenon of hydrophilic materials was ubiquitous in hybrid membranes (María Arsuaga et al. 2013; Miao et al. 2015; Wang et al. 2012b).

XPS and EDS had different capabilities, limitations, and depths of analysis, and these techniques might provide differing results from each other (Gorzalski et al. 2017; Xu et al. 2016). In order to understand the migration behavior of FGO, we attempted to use XPS, EDS, and indirect computation to detect oxygen contents in different depths of membranes and then analyzed FGO contents in the top layer, sublayer, and the whole membrane, respectively. The measurement depth of XPS and EDS was 1–10 nm and 0–5 μm, respectively. The oxygen content of the whole membrane included all of the oxygen of PVP and FGO. We used the oxygen count to evaluate the content of FGO and then investigated the migration behavior of FGO.

Table 2 showed the oxygen content trends in different depths of membranes: top layer (XPS) > sublayer (EDS) > whole membrane. The change of oxygen distribution in primary PVDF was mainly caused by PVP solvent diffusion. Oxygen mass fraction in top layer of PVDF/GO membrane was 8.75 wt%, higher than that of PVDF (3.7 wt%) and $(PVDF/FGO\text{-}n)_{max}$ (4.63 wt%). The main reason was that highly hydrophilic GO had a strong migration behavior. Previous studies showed that migration of amphiphilic copolymer during the immersion precipitation casting of the membrane was favored due to both enthalpic and entropic effects (Zhu et al. 2014b). The hydrogen bonding interactions between the hydroxyl or carboxyl group of FGO and water in the coagulation bath resulted in an enthalpic preference to exposing these hydrophilic groups to the water phase, on the membrane surface and inside pores (Asatekin et al. 2007; Sui et al. 2012; Zhu et al. 2014b). With a plasma treatment GO for 3 min, the oxygen contents in top layer and sublayer of

Table 2 Oxygen content of hybrid membranes in different depths

	PVDF	PVDF/GO	PVDF/FGO-3	PVDF/FGO-5	PVDF/FGO-10	PVDF/FGO-15	PVDF/FGO-20
Oxygen content in top layer (wt%)	3.7	8.75	4.59	4.59	4.63	4.4	3.93
Oxygen content in sublayer (wt%)	1.29	2.43	2.02	2.07	2.21	2.28	2.11
Oxygen content in Whole membrane (wt%)	0.90	1.25	1.19	1.15	1.11	1.08	1.00

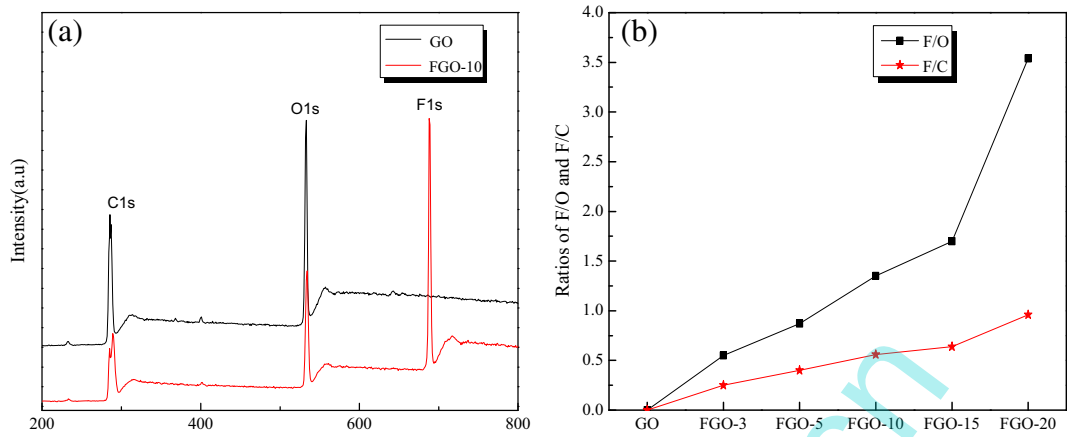

Fig. 1 **a** XPS survey spectra recorded on GO and FGO-10. **b** $R_{F/O}$ and $R_{F/C}$ of FGO

PVDF/FGO-3 membranes were 4.59 wt% and 2.02 wt%, respectively, similar to the oxygen content of PVDF/FGO-5 but far below the PVDF/GO (8.75% and 2.43%). It should be noted that the number of oxygen-containing groups was sharply reduced and few F atoms were grafted onto GO for a short plasma treatment time. As a result, the agglomeration of FGO-3 and FGO-5 was not relieved. Meanwhile, their migration behavior was not obvious during the phase inversion process when compared with GO.

To further quantitatively analyze the FGO-n distribution in membranes, we made the assumption that the contents of PVP in PVDF, PVDF/GO, and PVDF/FGO-n membranes were the same. After the exclusion of PVP, the oxygen of the whole membranes came only from either GO or FGO. We calculated the GO distribution in membrane as an example. In Table 2, the oxygen contents of PVDF/GO and neat PVDF membrane in the top layer could be denoted as $m_{(O/PVDF\text{-}GO))XPS}$ and $m_{(O/PVDF)XPS}$, respectively. Then, the oxygen mass fraction of GO in the membrane top layer could be obtained ($m_{(O/PVDF\text{-}GO)top} = m_{(O/PVDF\text{-}GO)XPS} - m_{(O/PVDF)XPS}$) by calculation. Similarly, by XPS analysis, the oxygen mass fraction of GO was expressed as $m_{(O/GO)}$. Therefore, the GO content distribution in the top layer of PVDF/GO membrane could be obtained by the formula (7). Analogously, the GO contents in sublayer

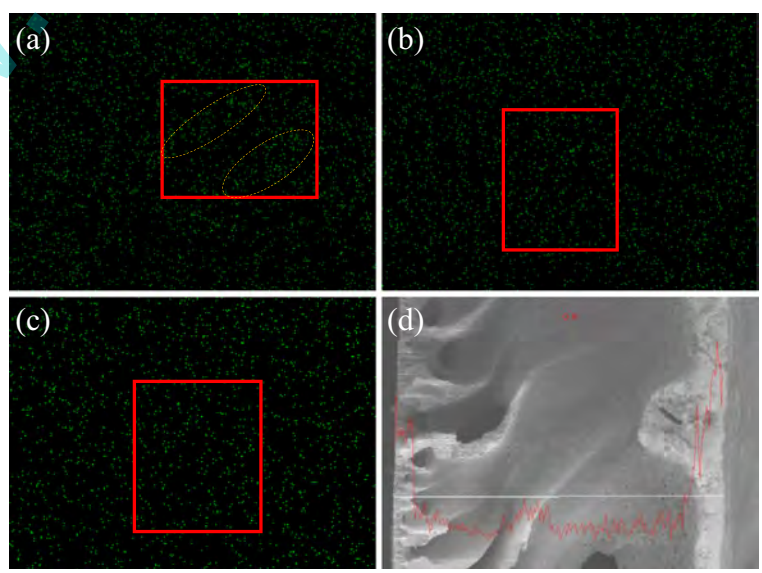

Fig. 2 The oxygen distribution of membrane surface. **a** PVDF/GO. **b** PVDF/FGO-10. **c** PVDF/FGO-20 and cross section with line scan. **d** PVDF/FGO-10

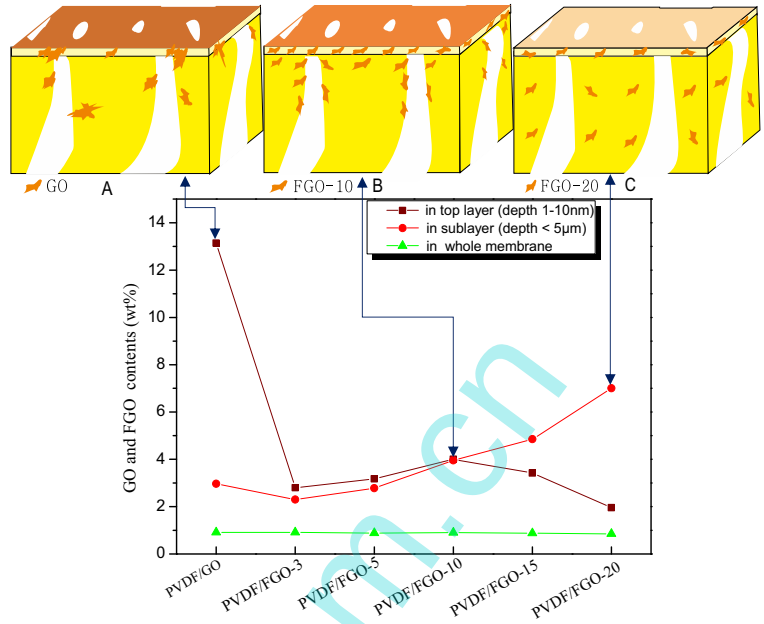

Fig. 3 GO and FGO contents at different depths of membranes and schematic illustration of distribution states of GO (**a**), FGO-10 (**b**), and FGO-20 (**c**)

($C_{(GO/PVDF\text{-}GO)sub}$) and the whole membrane ($C_{(GO/PVDF\text{-}GO)whole}$) could also be calculated as follows:

$$C_{\left(\mathrm{GO}/\mathrm{PVDF\text{-}GO}\right)\mathrm{top}} = \frac{m_{\left(\mathrm{O}/\mathrm{PVDF\text{-}GO}\right)\mathrm{top}}}{m_{\left(\mathrm{O}/\mathrm{GO}\right)}} \times 100\% \quad (7)$$

$$C_{\left(\mathrm{GO}/\mathrm{PVDF\text{-}GO}\right)\mathrm{sub}} = \frac{m_{\left(\mathrm{O}/\mathrm{PVDF\text{-}GO}\right)\mathrm{sub}}}{m_{\left(\mathrm{O}/\mathrm{GO}\right)}} \times 100\% \quad (8)$$

$$C_{\left(\mathrm{GO}/\mathrm{PVDF\text{-}GO}\right)\mathrm{whole}} = \frac{m_{\left(\mathrm{O}/\mathrm{PVDF\text{-}GO}\right)\mathrm{whole}}}{m_{\left(\mathrm{O}/\mathrm{GO}\right)}} \times 100\% \quad (9)$$

The FGO-n contents in different depths of membranes such as $C_{(FGO\text{-}n/PVDF\text{-}FGO\text{-}n)top}$, $C_{(FGO\text{-}n/PVDF\text{-}FGO\text{-}n)sub}$, and $C_{(FGO\text{-}n/PVDF\text{-}FGO\text{-}n)whole}$ were calculated by using the above-mentioned similar formulas (7–9). Figure 3 showed the contents of FGO-n in the top layer, sublayer, and the whole membrane. In comparison, the contents of GO, FGO-10, and FGO-20 in the top layer were 13.14, 4.00, and 1.96 wt%, respectively. The contents of GO, FGO-10, and FGO-20 in the sublayer were 2.97, 3.96, and 7.00 wt%, respectively. It was clear that the migration trends of FGO-n were different. With 10 min plasma treatment, the migration behavior of FGO-10 slightly increased (Fig. 3). This phenomenon could be explained by the increase of grafted F atoms potentially increasing compatibility, with the remaining oxygen functional groups in FGO-10 driving spontaneous migration to the membrane surface. With the increase of $R_{F/O}$ (Fig. 1b), FGO contents in the top layer and the sublayer of membranes were decreased and increased gradually, demonstrating the increasing dispersion and decreasing migration ability of FGO in membranes, as schematically illustrated in Fig. 3. As a result, we could achieve a balance point (near FGO-10) that allowed the synergistic effect of FGO migration and dispersion to reach equilibrium (Fig. 3 for the schematic illustration B). It could be inferred the closer to the equilibrium state of FGO in the matrix, the better the performance of membrane. Naturally, the permeability and antifouling performances of PVDF/FGO-10 and PVDF/FGO-15 membranes were relatively better by next performance tests.

Permeability and antifouling properties of membranes

The permeability and fouling behavior toward various membranes were investigated by dynamic filtration experiments using BSA as a model protein, and the results were depicted in Fig. 4. Figure 4a traced the typical

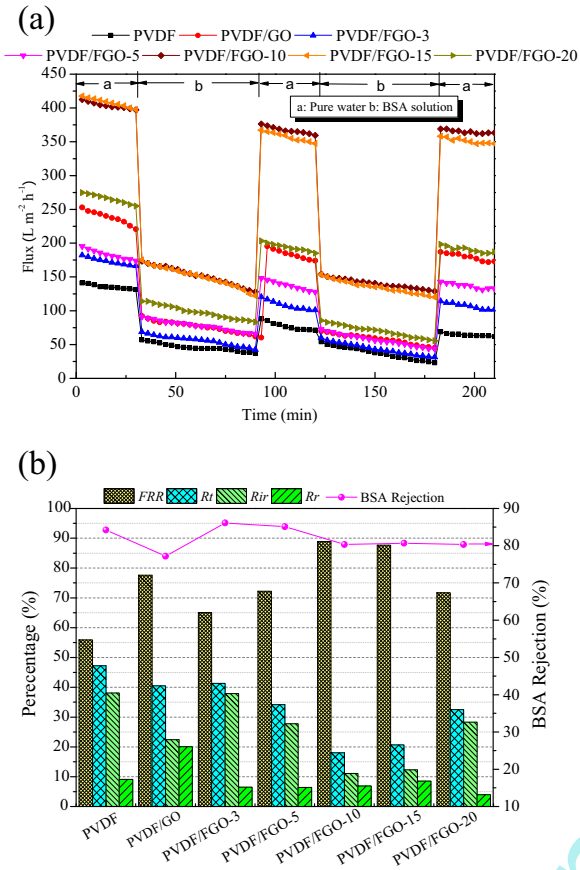

Fig. 4 Permeability and antifouling properties of membranes. **a** Time-dependent flux of various membranes under two cycles of BSA solution filtration. **b** Water flux recovery, fouling resistance ratio and BSA rejection of membranes

time-dependent fluxes of various membranes under two cycles of BSA solution filtration. Each filtration cycle includes three stages: water flux for 30 min, BSA solution flux for 60 min, and water flux for 30 min after 20 min washing with distilled water. It could be seen that the hybrid membranes showed higher fluxes as compared with pristine PVDF membranes. In marked contrast, the pure water flux of PVDF/FGO-10 membranes was 406.90 L m^{-2} h^{-1}, being 200.1% higher than that of PVDF membranes (134.89 L m^{-2} h^{-1}) and 67.3% higher than that of PVDF/GO membranes (243.23 L m^{-2} h^{-1}). When the pure water was replaced by BSA solution, flux declined sharply in BSA due to fouling and concentration polarization (Wang et al. 2009), and PVDF/FGO-10 as well as PVDF/FGO-15 membranes showed high permeation flux of BSA solution. With simple water rinsing, the permeation flux of membranes was recovered in different degrees but not completely reverted for all the membranes. This may be attributed to the BSA blocking membrane pores, which would be in agreement with the experience of Moghadam et al. (2015). The BSA rejection properties of the pristine and hybrid membranes were also presented in Fig. 4b. The rejection rates of membranes were all above 80%, expect for PVDF/GO (77.2%), and antifouling properties of hybrid membranes were found to first increase and then decrease with increasing $R_{F/O}$ of FGO. For PVDF/FGO-10 membranes, the FRR increased to 88.9%, a 59.0%, 14.6%, and 24.0% improvement compared with those of PVDF, PVDF/GO, and PVDF/FGO-20 membranes, respectively, as well as the Rir declined by 70.9%, 41.2%, and 25.7%, respectively. Naturally, the antifouling characteristics of PVDF/FGO-10 membranes were stable in the long-term operation (Fig. 4a). Those could be a result of FGO-10 dispersing and migrating in membranes, which played a critical role in elevating the antifouling property of hybrid membranes because the hydrophilicity and low surface free energy of membranes might be beneficial to entrap pollutants and more easily wash them away by water (Yang et al. 2011). However, the FRR of PVDF/FGO-3, PVDF/FGO-5, and PVDF/FGO-20 membranes were lower than that of PVDF/GO membranes, due to the fact that plenty of nanoparticles were aggregated or embedded in the polymer matrix, decreasing the hydrophilicity of membranes (Ji et al. 2012; Li et al. 2013; Shao et al. 2014).

AFM was used to probe the surface characteristic of membranes, as demonstrated in Fig.5. The surface roughness of the hybrid membranes, employing *Ra* and *RMS*, displayed an increase in trend compared with that of pristine PVDF membranes, in agreement with the results of Fig. S2 as discussed above. The *Ra* value increased from 32.7 nm (PVDF) to 42.7 nm (PVDF/GO), 36.3 nm (PVDF/FGO-3), 46.3 nm (PVDF/FGO-5), 65.5 nm (PVDF/FGO-10), 84.3 nm (PVDF/FGO-15), and 102 nm (PVDF/FGO-20), which was possibly due to the fast exchange of solvent and nonsolvent occurring during the phase inversion process because of the presence of FGO on the surface of hybrid membranes (Malinga et al. 2013; Wang et al. 2012c). Arisen from the adhesion force measured by AFM between the membrane surface and foulants, the magnitude of the adhesion force was directly related to the

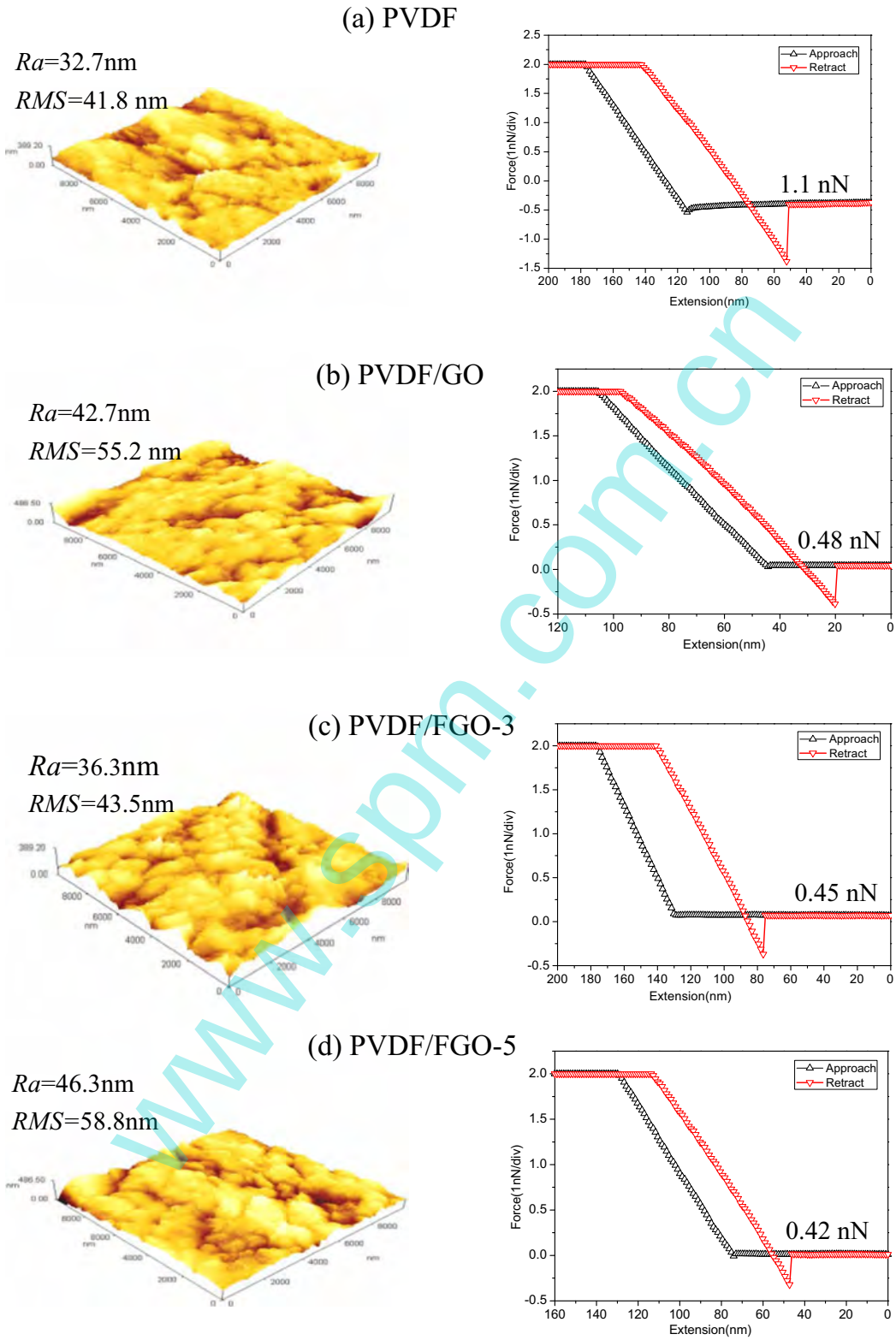

Fig. 5 AFM three-dimensional images (*left*) and force–extension curves recorded with a BSA-immobilized tip against (*right*). **a** Nascent PVDF, **b** PVDF/GO, **c** PVDF/FGO-3, **d** PVDF/FGO-5, **e** PVDF/FGO-10, **f** PVDF/FGO-15, and **g** PVDF/FGO-20

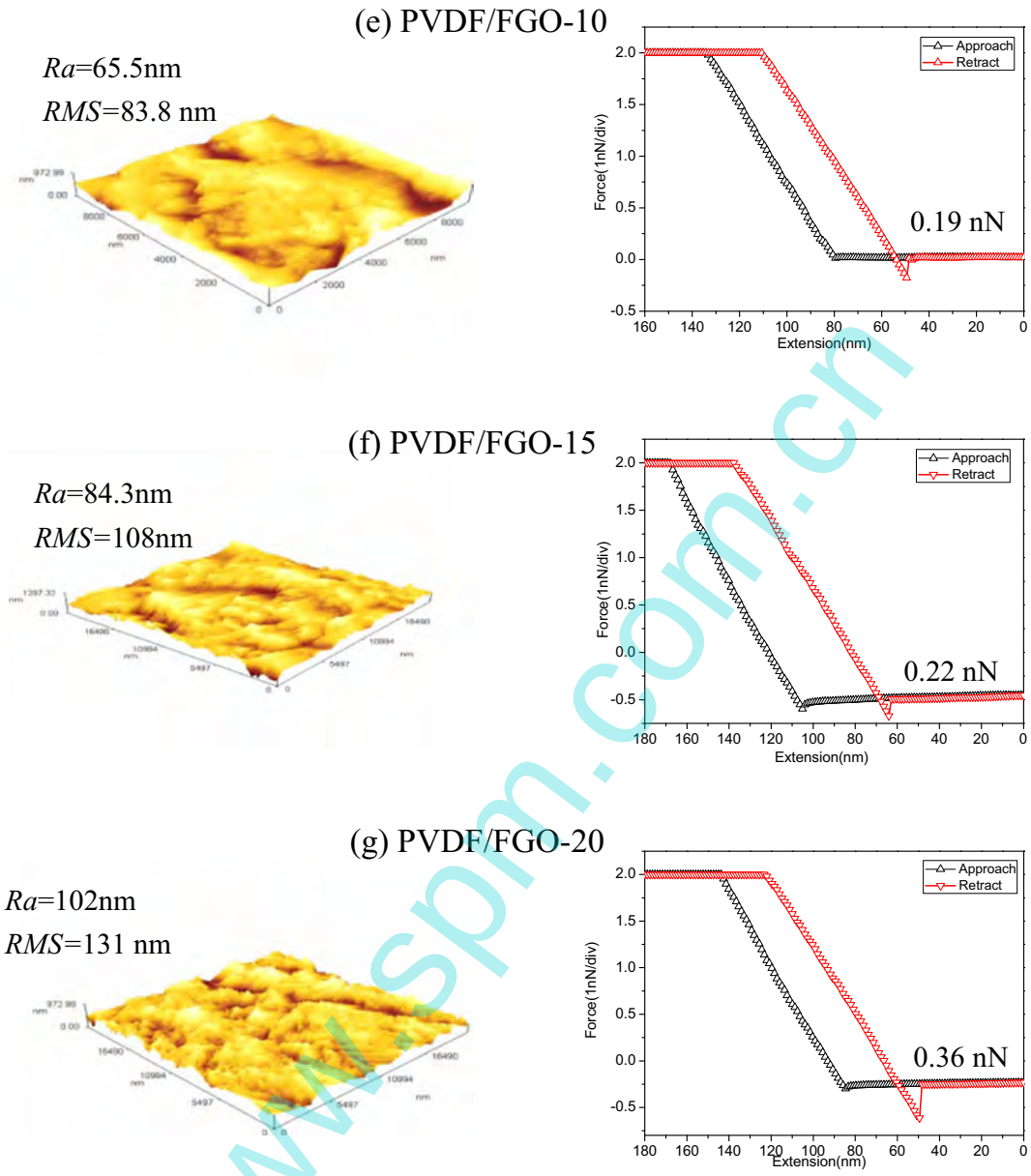

Fig. 5 (continued)

membrane fouling potential, which was a good indicator of membrane organic fouling (Johnson and Hilal 2015; Mo et al. 2012). Figure 5 (right) showed the force–extension curves recorded with a BSA-immobilized tip against various membrane surfaces, in which the inflection point in the retracting curve indicated the adhesion force between the membranes and BSA-immobilized tip (Liu et al. 2015c). The back process of protein-immobilized tip produced a relatively small adhesive force, which illustrated good antifouling performance. Figure 5a–g showed the membrane-foulant adhesion forces in the following order: PVDF (1.1 nN) > PVDF/FGO-3 > PVDF/GO > PVDF/FGO-5 > PVDF/FGO-20 > PVDF/FGO-15 > PVDF/FGO-10 (0.19 nN). It was clear that PVDF/FGO-10 exhibited the lowest adhesion force, which could be inferred that FGO-10 played a leading role in the optimal of membrane properties due to low surface free energy of fluorine-containing segments (Cui et al. 2014) and the synergistic effect of FGO-10 migration and dispersion

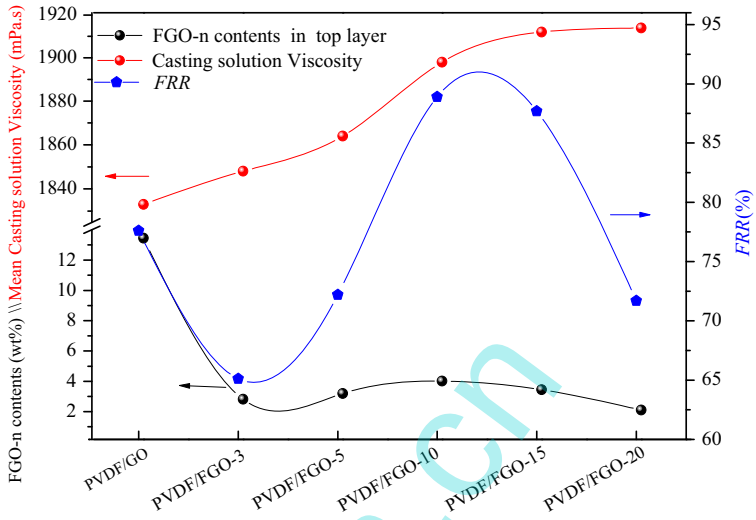

Fig. 6 Compatibility (*red*), migration behavior (*black*), and antifouling properties of hybrid membranes (*blue*)

in phase inversion process (Fig. 3). It was generally agreed that a membrane with smoother surface possessed greater antifouling capability (Rana and Matsuura 2010). However, if the increase in roughness was caused by the enrichment of hydrophilic nanomaterials and fluorine-containing segments on the membrane surface, it improved the membrane surface hydrophilicity and reduced surface free energy although the roughness was high (Wu et al. 2015). Consequently, the hybrid membranes were undoubtedly beneficial to promote water permeability and antifouling properties.

Effect of FGO compatibility and migration behavior on the antifouling properties of hybrid membranes

Figure 6 showed two factors of FGO, dispersion and migration, influencing on the optimal performance of hybrid membranes. With prolonged plasma treatment time, it could be seen that the increased casting solution viscosity of PVDF/FGO-n indicated an increased FGO compatibility in membranes. The decreased FGO content in the top layer revealed a reduced FGO migration ability in membranes. As shown in Fig. 6, it could be

Table 3 Comparison of the comprehensive performance of hybrid membranes in this work and other recent literatures

Membrane	Optimum dosage (wt%)	Water flux ($Lm^{-2}\ h^{-1}\ bar^{-1}$)	BSA rejection (%)	FRR (%)	Ref.
PES-SiO_2[b]	5	141.8	94.6	84.4	Zhu et al. (2014a)
PSF/TiO_2-g-HEMA[a]	2	148.77	93.0	81.7	Zhang et al. (2013a)
PSF-SiO_2/GO[a]	0.3	~185	98	72	Wu et al. (2014)
PS/GO[c]	0.005	70	~75	–	Meng et al. (2015)
PVDF/GO[a]	1	163	83.7	85.1	Zhang et al. (2013b)
PVDF-GO/OMWCNTs[a]	1	203	81.6	80.4	Zhang et al. (2013b)
PVDF/GO[a]	0.5	104.3	85	–	Chang et al. (2014)
PVDF-PDAAQ/rGO[b]	1.5	~68	77.4	86.8	Liu et al. (2015a)
PSF-iGO[a]	0.05	140	95	40.3	Zhao et al. (2013a)
PVDF/GO[a]	0.15	243.2	77.2	77.6	This work
PVDF/FGO-10[a]	0.15	406.9	80.7	88.9	

[a] The dosage of nanomaterials is based on the total weight of polymer casting solution

[b] The dosage of inorganic nanomaterials is based on the weight of polymer

[c] The dosage of nanomaterials is based on the concentration of coagulation bath

inferred that the performance of PVDF/FGO-10 was better than that of PVDF/GO and PVDF/FGO-20, although GO possessed the most significant migration behavior in PVDF matrix and FGO-20 possessed the best compatibility with the PVDF in all system studied FGO. Finally, the comprehensive performance of PVDF/FGO membranes in this work was compared to other hybrid membranes from recent literatures, and the data were presented in Table 3. From the data, it could clearly be seen that the PVDF/FGO-10 membranes offered an improved performance compared with other hybrid membranes, illustrating that the synergistic effect of FGO-10 migration and dispersion in membrane was obvious, and near FGO-10 the synergistic effect led to a maximum, which could play an important role in optimizing membrane performance.

Conclusions

In order to analyze the effect of nanomaterials on permeability and antifouling properties of hybrid membranes, we designed different $R_{F/O}$ of FGO by plasma treatment and successfully prepared novel PVDF hybrid membranes containing FGO with good dispersion and migration in the matrix. The following can be highlighted from the experimental:

1. With increasing plasma treatment time, the $R_{F/O}$ of FGO increased dramatically and the viscosity of PVDF/FGO casting solution gradually enhanced, indicating the enhanced dispersion stability of FGO in matrix. FGO contents in the top layer of membranes declined from 13.14 wt% (PVDF/GO) to 1.96 wt% (PVDF/FGO-20), while FGO-n contents in the sublayer gradually increased, indicating that the migration driving force of FGO gradually decreased because of the reduction of oxygen-containing functional groups.
2. The pure water flux and FRR of PVDF/FGO-10 membranes were up to 406.90 L m^{-2} h^{-1} and 88.9%, being 67.3% and 14.6% and 52.5% and 24.0% higher than those of PVDF/GO and PVDF/FGO-20 membranes, respectively. The hybrid membranes exhibited much higher roughness values but lower adhesion forces with BSA than pristine membranes by AFM analysis, implying the migration and enrichment of FGO (especially FGO-10, $R_{F/O}$ = 1.35) on membrane surface during the phase inversion process.
3. These performances demonstrated that PVDF/FGO-10 outperformed PVDF/GO and PVDF/FGO-20 membranes, although the migration and dispersion of FGO-10 were maintained at a moderate level in this case. This is because both the dispersion and migration of FGO (near $R_{F/O}$ = 1.35) in the membrane matrix have significant effect to make the best use of nanomaterials, possibly promoting the performance of hybrid membranes to reach the maximum.

Acknowledgements The work was funded by the National Natural Science Foundation of China (11575126), the Qaidam Salt Chemical Joint Fund of National Natural Science Foundation of China, People's Government of Qinghai Province (U1607117), the Natural Science Foundation of Tianjin (16JCZDJC36400), and the Science and Technology Plans of Tianjin (15PTSYJC00230).

Compliance with ethical standards

Conflict of interest The authors declared that they have no conflicts of interest to this work.

References

Asatekin A, Kang S, Elimelech M, Mayes AM (2007) Antifouling ultrafiltration membranes containing polyacrylonitrile-graft-poly(ethylene oxide) comb copolymer additives. J Membr Sci 298(1–2):136–146. doi:10.1016/j.memsci.2007.04.011

Chang X, Wang Z, Quan S, Xu Y, Jiang Z, Shao L (2014) Exploring the synergetic effects of graphene oxide (GO) and polyvinylpyrrodione (PVP) on poly(vinylylidenefluoride) (PVDF) ultrafiltration membrane performance. Appl Surf Sci 316:537–548. doi:10.1016/j.apsusc.2014.07.202

Chen W, Su Y, Peng J, Dong Y, Zhao X, Jiang Z (2011) Engineering a robust, versatile amphiphilic membrane surface through forced surface segregation for ultralow flux-decline. Adv Funct Mater 21(1):191–198. doi:10.1002/adfm.201001384

Cui Z, Drioli E, Lee YM (2014) Recent progress in fluoropolymers for membranes. Prog Polym Sci 39(1):164–198. doi:10.1016/j.progpolymsci.2013.07.008

Goh PS, Ng BC, Lau WJ, Ismail AF (2014) Inorganic nanomaterials in polymeric ultrafiltration membranes for water treatment. Sep Purif Rev 44(3):216–249. doi:10.1080/15422119.2014.926274

Gorzalski AS, Donley C, Coronell O (2017) Elemental composition of membrane foulant layers using EDS, XPS, and RBS. J Membr Sci 522:31–44. doi:10.1016/j.memsci.2016.08.055

Greenlee LF, Rentz NS (2016) Influence of nanoparticle processing and additives on PES casting solution viscosity and cast membrane characteristics. Polymer 103:498–508. doi:10.1016/j.polymer.2016.04.021

Hashim NA, Liu F, Li K (2009) A simplified method for preparation of hydrophilic PVDF membranes from an amphiphilic graft copolymer. J Membr Sci 345(1–2):134–141. doi:10.1039/C5TA05306D

Hong J, He Y (2014) Polyvinylidene fluoride ultrafiltration membrane blended with nano-ZnO particle for photo-catalysis self-cleaning. Desalination 332(1):67–75. doi:10.1016/j.desal.2013.10.026

Ji Y-L, An Q-F, Zhao Q, Sun W-D, Lee K-R, Chen H-L, Gao C-J (2012) Novel composite nanofiltration membranes containing zwitterions with high permeate flux and improved antifouling performance. J Membr Sci 390-391:243–253. doi:10.1016/j.memsci.2011.11.047

Jiang B, Tao PH, Huang YD (2014) Study of the adsorption performance and preparation of functional nano-silica pigment particles. Dyes Pigments 104:169–174. doi:10.1016/j.dyepig.2014.01.009

Johnson D, Hilal N (2015) Characterisation and quantification of membrane surface properties using atomic force microscopy: a comprehensive review. Desalination 356:149–164. doi:10.1016/j.desal.2014.08.019

Li Q, Q-y B, Lin H-H, Bian L-X, Wang X-L (2013) A novel ultrafiltration (UF) membrane with controllable selectivity for protein separation. J Membr Sci 427:155–167. doi:10.1016/j.memsci.2012.09.010

Li X, Li J, Fang X, Bakzhan K, Wang L, Van der Bruggen B (2016) A synergetic analysis method for antifouling behavior investigation on PES ultrafiltration membrane with self-assembled TiO2 nanoparticles. J Colloid Interf Sci 469:164–176. doi:10.1016/j.jcis.2016.02.002

Liang S, Xiao K, Mo Y, Huang X (2012) A novel ZnO nanoparticle blended polyvinylidene fluoride membrane for anti-irreversible fouling. J Membr Sci 394-395:184–192. doi:10.1016/j.memsci.2011.12.040

Liu HY, Zhang GQ, Zhao CQ, Liu JD, Yang FL (2015a) Hydraulic power and electric field combined antifouling effect of novel conductive poly(aminoanthraquinone)/reduced graphene oxide nanohybrid blended PVDF ultrafiltration membrane. J Mater Chem A 3:20277–20287. doi:10.1039/C5TA05306D

Liu Y, Su Y, Li Y, Zhao X, Jiang Z (2015b) Improved antifouling property of PVDF membranes by incorporating an amphiphilic block-like copolymer for oil/water emulsion separation. RSC Adv 5(27):21349–21359. doi:10.1039/c4ra16290k

Liu Y et al (2015c) Investigation of antifouling universality of polyvinyl formal (PVF) membranes utilizing atomic force microscope (AFM) force curves. RSC Adv 5(46):36894–36901. doi:10.1039/c5ra05380c

Ma J et al (2013) Role of oxygen-containing groups on MWCNTs in enhanced separation and permeability performance for PVDF hybrid ultrafiltration membranes. Desalination 320:1–9. doi:10.1016/j.desal.2013.04.012

Malinga SP, Arotiba OA, Krause RWM, Mapolie SF, Diallo MS, Mamba BB (2013) Composite polyester membranes with embedded dendrimer hosts and bimetallic Fe/Ni nanoparticles: synthesis, characterisation and application to water treatment. J Nanopart Res 15(6). doi:10.1007/s11051-013-1698-y

María Arsuaga J, Sotto A, del Rosario G, Martínez A, Molina S, Teli SB, de Abajo J (2013) Influence of the type, size, and distribution of metal oxide particles on the properties of nanocomposite ultrafiltration membranes. J Membr Sci 428:131–141. doi:10.1016/j.memsci.2012.11.008

Meng N, Wang Z, Low Z-X, Zhang Y, Wang H, Zhang X (2015) Impact of trace graphene oxide in coagulation bath on morphology and performance of polysulfone ultrafiltration membrane. Sep Purif Technol 147:364–371. doi:10.1016/j.seppur.2015.02.043

Meng N, Priestley RCE, Zhang Y, Wang H, Zhang X (2016) The effect of reduction degree of GO nanosheets on microstructure and performance of PVDF/GO hybrid membranes. J Membr Sci 501:169–178. doi:10.1016/j.memsci.2015.12.004

Miao R, Wang L, Wang X, Lv Y, Gao Z, Mi N, Liu T (2015) Preparation of a polyvinylidene fluoride membrane material probe and its application in membrane fouling research. Desalination 357:171–177. doi:10.1016/j.desal.2014.11.029

Mo Y, Tiraferri A, Yip NY, Adout A, Huang X, Elimelech M (2012) Improved antifouling properties of polyamide nanofiltration membranes by reducing the density of surface carboxyl groups. Environ Sci Technol 46:13253–13261. doi:10.1021/es303673p

Moghadam MT et al (2015) Improved antifouling properties of TiO2/PVDF nanocomposite membranes in UV-coupled ultrafiltration. J Appl Polym Sci 41731:1–13. doi:10.1002/app.41731

Pang R, Li X, Li J, Lu Z, Sun X, Wang L (2014) Preparation and characterization of ZrO2/PES hybrid ultrafiltration membrane with uniform ZrO2 nanoparticles. Desalination 332(1):60–66. doi:10.1016/j.desal.2013.10.024

Rahimpour A, Jahanshahi M, Khalili S, Mollahosseini A, Zirepour A, Rajaeian B (2012) Novel functionalized carbon nanotubes for improving the surface properties and performance of polyethersulfone (PES) membrane. Desalination 286:99–107. doi:10.1016/j.desal.2011.10.039

Rana D, Matsuura T (2010) Surface modifications for antifouling membranes. Chem Rev 110:2448–2471. doi:10.1021/cr800208y

Shao L, Wang ZX, Zhang YL, Jiang ZX, Liu YY (2014) A facile strategy to enhance PVDF ultrafiltration membrane performance via self-polymerized polydopamine followed by hydrolysis of ammonium fluotitanate. J Membr Sci 461:10–21. doi:10.1016/j.memsci.2014.03.006

Shi C et al (2012) Monitoring influence of chemical preparation procedure on the structure of graphene nanosheets. Phys E 44(7–8):1420–1424. doi:10.1016/j.physe.2012.03.004

Sui Y, Wang Z, Gao X, Gao C (2012) Antifouling PVDF ultrafiltration membranes incorporating PVDF-g-PHEMA additive via atom transfer radical graft polymerizations. J Membr Sci 413-414:38–47. doi:10.1016/j.memsci.2012.03.055

Sukitpaneenit P, Chung T-S (2009) Molecular elucidation of morphology and mechanical properties of PVDF hollow fiber membranes from aspects of phase inversion, crystallization and rheology. J Membr Sci 340(1–2):192–205. doi:10.1016/j.memsci.2009.05.029

Tan X, Tan SP, Teo WK, Li K (2006) Polyvinylidene fluoride (PVDF) hollow fibre membranes for ammonia removal from water. J Membr Sci 271(1–2):59–68. doi:10.1016/j.memsci.2005.06.057

Vatanpour V, Madaeni SS, Rajabi L, Zinadini S, Derakhshan AA (2012) Boehmite nanoparticles as a new nanofiller for preparation of antifouling mixed matrix membranes. J Membr Sci 401-402:132–143. doi:10.1016/j.memsci.2012.01.040

Wang L, Y-l S, Zheng L, Chen W, Jiang Z (2009) Highly efficient antifouling ultrafiltration membranes incorporating zwitterionic poly([3-(methacryloylamino)propyl]-dimethyl(3-sulfopropyl) ammonium hydroxide). J Membr Sci 340(1–2):164–170. doi:10.1016/j.memsci.2009.05.027

Wang P, Ma J, Wang Z, Shi F, Liu Q (2012a) Enhanced separation performance of PVDF/PVP-g-MMT nanocomposite ultrafiltration membrane based on the NVP-grafted polymerization modification of montmorillonite (MMT). Langmuir 28(10): 4776–4786. doi:10.1021/la203494z

Wang X, Xing W, Zhang P, Song L, Yang H, Hu Y (2012b) Covalent functionalization of graphene with organosilane and its use as a reinforcement in epoxy composites. Compos Sci Technol 72(6):737–743. doi:10.1016/j.compscitech.2012.01.027

Wang Z, Yu H, Xia J, Zhang F, Li F, Xia Y, Li Y (2012c) Novel GO-blended PVDF ultrafiltration membranes. Desalination 299:50–54. doi:10.1016/j.desal.2012.05.015

Wang Z, Wei Y-M, Xu Z-L, Cao Y, Dong Z-Q, Shi X-L (2016) Preparation, characterization and solvent resistance of γ-Al2O3/α-Al2O3 inorganic hollow fiber nanofiltration membrane. J Membr Sci 503:69–80. doi:10.1016/j.memsci.2015.12.039

Wu H, Tang B, Wu P (2010) Novel ultrafiltration membranes prepared from a multi-walled carbon nanotubes/polymer composite. J Membr Sci 362(1–2):374–383

Wu H, Tang B, Wu P (2014) Development of novel SiO2–GO nanohybrid/polysulfone membrane with enhanced performance. J Membr Sci 451:94–102. doi:10.1016/j.memsci.2013.09.018

Wu T, Zhou B, Zhu T, Shi J, Xu Z, Hu C, Wang J (2015) Facile and low-cost approach towards a PVDF ultrafiltration membrane with enhanced hydrophilicity and antifouling performance via graphene oxide/water-bath coagulation. RSC Adv 5(11): 7880–7889. doi:10.1039/c4ra13476a

Xu Z et al (2014) Organosilane-functionalized graphene oxide for enhanced antifouling and mechanical properties of polyvinylidene fluoride ultrafiltration membranes. J Membr Sci 458:1–13. doi:10.1016/j.memsci.2014.01.050

Xu Z et al (2016) Manipulating migration behavior of magnetic graphene oxide via magnetic field induced casting and phase separation toward high-performance hybrid ultrafiltration membranes. ACS Appl Mater Inter 8(28):18418–18429. doi:10.1021/acsami.6b04083

Yang X et al (2011) Preparation of the antifouling microfiltration membranes from poly(N,N-dimethylacrylamide) grafted poly(vinylidene fluoride) (PVDF) powder. J Mater Chem 21(32):11908. doi:10.1039/c1jm11348h

Yeow ML, Liu YT, Li K (2004) Morphological study of poly(vinylidene fluoride) asymmetric membranes: effects of the solvent, additive, and dope temperature. J Appl Polym Sci 92(3). doi:10.1002/app.20141

Zhang P-Y, Xu Z-L, Yang H, Wei Y-M, Wu W-Z (2013a) Fabrication and characterization of PVDF membranes via an in situ free radical polymerization method. Chem Eng Sci 97:296–308. doi:10.1016/j.ces.2013.03.058

Zhang G, Lu S, Zhang L, Meng Q, Shen C, Zhang J (2013b) Novel polysulfone hybrid ultrafiltration membrane prepared with TiO2-g-HEMA and its antifouling characteristics. J Membr Sci 436:163–173. doi:10.1016/j.memsci.2013.02.009

Zhang J et al (2013c) Improved hydrophilicity, permeability, antifouling and mechanical performance of PVDF composite ultrafiltration membranes tailored by oxidized low-dimensional carbon nanomaterials. J Mater Chem A 1(9): 3101. doi:10.1016/j.memsci.2013.07.064

Zhang J et al (2013d) Synergetic effects of oxidized carbon nanotubes and graphene oxide on fouling control and anti-fouling mechanism of polyvinylidene fluoride ultrafiltration membranes. J Membr Sci 448:81–92. doi:10.1016/j.memsci.2013.07.064

Zhang W, Zhang Y, Fan R, Lewis R (2016) A facile TiO2/PVDF composite membrane synthesis and their application in water purification. J Nanopart Res 18(1). doi:10.1007/s11051-015-3281-1

Zhao H, Wu L, Zhou Z, Zhang L, Chen H (2013a) Improving the antifouling property of polysulfone ultrafiltration membrane by incorporation of isocyanate-treated graphene oxide. Phys Chem Chem Phys 15(23):9084–9092. doi:10.1039/c3cp50955a

Zhao Y-F, Zhu L-P, Yi Z, Zhu B-K, Xu Y-Y (2013b) Improving the hydrophilicity and fouling-resistance of polysulfone ultrafiltration membranes via surface zwitterionicalization mediated by polysulfone-based triblock copolymer additive. J Membr Sci 440:40–47. doi:10.1016/j.memsci.2013.03.064

Zhao Y et al (2013c) Effect of graphite oxide and multi-walled carbon nanotubes on the microstructure and performance of PVDF membranes. Sep Purif Technol 103:78–83. doi:10.1016/j.seppur.2012.10.012

Zhao X, Su Y, Li Y, Zhang R, Zhao J, Jiang Z (2014) Engineering amphiphilic membrane surfaces based on PEO and PDMS segments for improved antifouling performances. J Membr Sci 450:111–123. doi:10.1016/j.memsci.2013.08.044

Zhou B et al (2015) Tailoring the chemical composition and dispersion behavior of fluorinated graphene oxide via CF4 plasma. J Nanopart Res 17(3). doi:10.1007/s11051-015-2946-0

Zhu LJ, Zhu LP, Jiang JH, Yi Z, Zhao YF, Zhu BK, Xu YY (2014a) Hydrophilic and anti-fouling polyethersulfone ultrafiltration membranes with poly(2-hydroxyethyl methacrylate) grafted silica nanoparticles as additive. J Membr Sci 451:157–168. doi:10.1016/j.memsci.2013.09.053

Zhu LJ, Zhu LP, Zhao YF, Zhu BK, Xu YY (2014b) Anti-fouling and anti-bacterial polyethersulfone membranes quaternized from the additive of poly(2-dimethylamino ethyl methacrylate) grafted SiO2 nanoparticles. J Mater Chem A 2(37): 15566. doi:10.1039/c4ta03199g

Zhu J, Zhao X, He C (2015) Zwitterionic SiO2 nanoparticles as novel additives to improve the antifouling properties of PVDF membranes. RSC Adv 5(66):53653–53659. doi:10.1039/c5ra05571g

Zhu LJ, Zhu LP, Zhang PB, Zhu BK, Xu YY (2016) Surface zwitterionicalization of poly(vinylidene fluoride) membranes from the entrapped reactive core-shell silica nanoparticles. J Colloid Interf Sci 468:110–119. doi:10.1016/j.jcis.2016.01.043